

CineMyoPS: Segmenting Myocardial Pathologies from Cine Cardiac MR

Wangbin Ding, Lei Li, Junyi Qiu, Bogen Lin, Mingjing Yang, Liqin Huang, Lianming Wu, Sihan Wang, Xiahai Zhuang

Abstract—Myocardial infarction (MI) is a leading cause of death worldwide. Late gadolinium enhancement (LGE) and T2-weighted cardiac magnetic resonance (CMR) imaging can respectively identify scarring and edema areas, both of which are essential for MI risk stratification and prognosis assessment. Although combining complementary information from multi-sequence CMR is useful, acquiring these sequences can be time-consuming and prohibitive, e.g., due to the administration of contrast agents. Cine CMR is a rapid and contrast-free imaging technique that can visualize both motion and structural abnormalities of the myocardium induced by acute MI. Therefore, we present a new end-to-end deep neural network, referred to as CineMyoPS, to segment myocardial pathologies, i.e., scars and edema, solely from cine CMR images. Specifically, CineMyoPS extracts both motion and anatomy features associated with MI. Given the interdependence between these features, we design a consistency loss (resembling the co-training strategy) to facilitate their joint learning. Furthermore, we propose a time-series aggregation strategy to integrate MI-related features across the cardiac cycle, thereby enhancing segmentation accuracy for myocardial pathologies. Experimental results on a multi-center dataset demonstrate that CineMyoPS achieves promising performance in myocardial pathology segmentation, motion estimation, and anatomy segmentation.

Index Terms—Myocardial Pathology Segmentation, Cine CMR, Motion Estimation, Contrast-Free

I. INTRODUCTION

The incidence of myocardial infarction (MI) is rising worldwide [1]. MI is typically caused by blockages in the coronary arteries, leading to the formation of the area at risk (AAR) in the myocardium. In acute MI cases, the AAR typically consists of scarring and edema regions [2]. Clinicians can calculate the myocardial salvage index and assess the prognosis of MI patients based on these two regions [3]. Thus, AAR quantification is critical for clinical applications.

Cardiac magnetic resonance (CMR) imaging techniques can visualize myocardial structure, motion, and pathological changes [4], making them invaluable for quantifying the AAR in MI patients [5]. As shown in the left panel of Fig. 1, late gadolinium enhancement (LGE) CMR visualizes scarring areas, while T2-weighted (T2w) CMR identifies edema [5]. However, these techniques face clinical limitations. For instance, the average acquisition time of multi-sequence CMR (MS-CMR), comprising T2w, first-pass perfusion, cine, and LGE, is approximately 32 ± 8 minutes [6], making it impractical for severe acute MI cases. In particular, acquiring the LGE sequence is time-consuming, accounting for approximately 50% of the total examination duration [7]. Moreover, the potential harm of gadolinium deposition remains under debate [8], and there is a risk of cross-reactivity with other macrocyclic contrast agents [9]. These limitations highlight the need for alternative methods that require fewer CMR sequences and avoid the use of contrast agents [10].

MI can induce abnormal motion patterns in the myocardium, and the analysis of these patterns has been widely investigated for infarction localization. Medical imaging modalities, such as cine CMR images, are capable of capturing these motion abnormalities as well as structural malformations, as shown in the right panel of Fig. 1. Various methods have been proposed to localize infarcts based on myocardial deformation patterns, with the aim of reducing the risks associated with contrast agents. One of the most straightforward approaches is to threshold the deformation patterns [11]. To achieve better localization accuracy, more advanced machine learning techniques have been employed, such as kernel regression [12], dictionary learning [13], and random forests [14]. In addition, due to the complexity of deformation patterns, strain parameters [15], [16] and embedding techniques [17], [18] have been incorporated to improve scar identification performance.

Corresponding authors: M. Yang, L. Huang, L. Wu and X. Zhuang. This work was supported by the National Natural Science Foundation of China (62401148, 62372115, 62271149); the Shanghai Municipal Education Commission-Artificial Intelligence Initiative to Promote Research Paradigm Reform and Empower Disciplinary Advancement Plan (24KXZNA13); the Research Initiation Project of Fujian Medical University (XRCZX2024003); the Science and Technology Project of Fujian Province (2020Y9037, 2021Y9220, 2020Y9091, 2022Y4014, 2024J01353).

W. Ding is with the School of Medical Imaging, Fujian Medical University, Fuzhou 350117, China. (dingwangbin@fjmu.edu.cn)

B. Lin, L. Huang and M. Yang are with the College of Physics and Information Engineering, Fuzhou University, Fuzhou 350117, China (221127167@fzu.edu.cn; hlq@fzu.edu.cn; yangmj5@fzu.edu.cn).

L. Li is with the Department of Biomedical Engineering, National University of Singapore, Singapore (lei.li@nus.edu.sg).

J. Qiu, S. Wang and X. Zhuang are with the School of Data Science, Fudan University, Shanghai, China (qiy980811@gmail.com; 21110980009@m.fudan.edu.cn; zxh@fudan.edu.cn).

L. Wu is with the Department of Radiology, Renji Hospital, School of Medicine, Shanghai Jiao Tong University, Shanghai, China (wlmssmu@126.com)

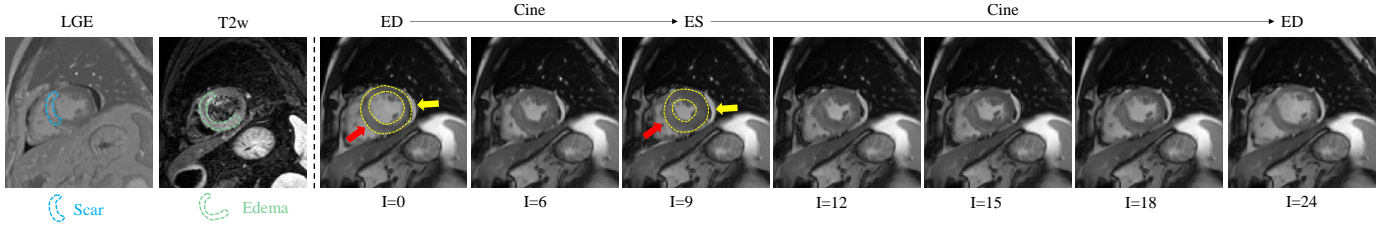


Fig. 1: Representative LGE, T2w, and cine CMR images from an MI patient. The infarcted myocardium remains relatively stationary (indicated by red arrows), whereas the viable myocardium exhibits noticeable deformation (indicated by yellow arrows). This observation suggests that myocardial pathologies can induce abnormal motion patterns in the myocardium. ED: end-diastolic frame, ES: end-systolic frame.

Recently, deep neural network (DNN) techniques have improved non-contrast quantification of myocardial pathology by leveraging cine CMR images [19]–[21]. These methods can be categorized into three groups:

- Motion estimation-based methods [20]: These methods establish associations between motion fields and scars using DNN. However, they rely on an external optical flow algorithm [22] to extract wall motion from cine CMR images.
- Spatio-temporal convolution network-based methods [19]: Since cine CMR images capture both spatial and temporal information of the myocardium, these methods employ convolution layers, such as ConvLSTM [23] and 3D Unet [24], to extract underlying spatio-temporal features for scar prediction.
- Synthesis-contrast-based methods [21]: These methods utilize conditional generative adversarial networks (GANs) [25] to synthesize LGE-equivalent images, from which scars can be directly extracted using existing segmentation methods, such as Unet [26].

Even though cine CMR provides a fast and contrast-free way for myocardial pathology quantification, existing cine CMR-based methods primarily focus on scar segmentation. *Limited attention has been paid to edema pathology*, which is critical in identifying the potential rescued heart tissue after an intervention [27]. Nevertheless, several studies have demonstrated that cine CMR sequences exhibit internal consistency in the assessment of edema in the myocardium, providing a new opportunity to jointly assess myocardial scars and edema from the cine CMR [28], [29].

In this work, we propose an end-to-end myocardial pathology segmentation (MyoPS) network, referred to as CineMyoPS, based on DNN techniques. To the best of our knowledge, CineMyoPS is the first fully automatic network for joint scars and edema segmentation from cine CMR images. Specifically, it introduces a motion estimation module to track myocardial movements and a segmentation module to extract anatomical structures from cine CMR images. Given that both modules rely on structural features, we introduce a consistency loss to improve the feature extraction of the two modules. To further enhance MyoPS performance, we propose a time-series aggregation strategy that flexibly fuses myocardial motion, anatomy, and texture features across cardiac cycles. Overall, CineMyoPS is an extension of motion estimation-

based methods, as it captures various features, including motion, to enhance MyoPS. Additionally, it is inspired by spatio-temporal methods, specifically leveraging time-series information to enhance MyoPS across cardiac cycles.

II. METHOD

Fig. 2 shows the network architecture of CineMyoPS, which consists of three modules: a myocardial motion estimation module (see Section II-A), an anatomy segmentation module (see Section II-B), and a MyoPS module (see Section II-C). CineMyoPS aggregates multiple types of features along a cardiac cycle and predicts myocardial pathologies, including scars and edema, in a reference image space.

A. Myocardial Motion Estimation

The extent of wall-motion abnormality is strongly correlated with the AAR and infarction size in MI patients [30]. We introduce a motion estimation module to capture motion from cine CMR sequences. Let $\mathbf{I} = \{I_i | i = 1 \dots n\}$ be a cine CMR sequence with n frames. We set the end-diastolic (ED) frame of \mathbf{I} as a common reference image (*i.e.*, I_r), and introduce a network to estimate the motion between I_r and each I_i .

The backbone of the motion estimation module is a U-shaped registration subnetwork [31]. It takes I_i and I_r as input and predicts a dense displacement field (DDF) between them. Formally, the motion estimation module can be defined as follows:

$$\Phi_i = \mathcal{F}_{motion}(I_r, I_i), \quad (1)$$

where Φ_i is the predicted DDF. We can transform I_i to I_r by using the corresponding DDF as follows:

$$\tilde{I}_i = I_i \otimes \Phi_i, \quad (2)$$

where \otimes denotes the image transform operation, and each element in \tilde{I}_i is calculated as follows:

$$\tilde{I}_i(\mathbf{c}) = I_i(\mathbf{c} + \Phi_i(\mathbf{c})), \quad (3)$$

where \mathbf{c} denotes a spatial point and $\Phi_i(\mathbf{c})$ represents the corresponding displacement at \mathbf{c} . Note that Φ_i is defined within the reference image space. Each element of Φ_i , *e.g.* $\Phi_i(\mathbf{c})$, represents the movement of \mathbf{c} from the time point of I_r to I_i , as shown in Fig. 3. By estimating the DDF between I_i and I_r , we obtain the motion pattern of \mathbf{c} , which can further be applied to MyoPS.

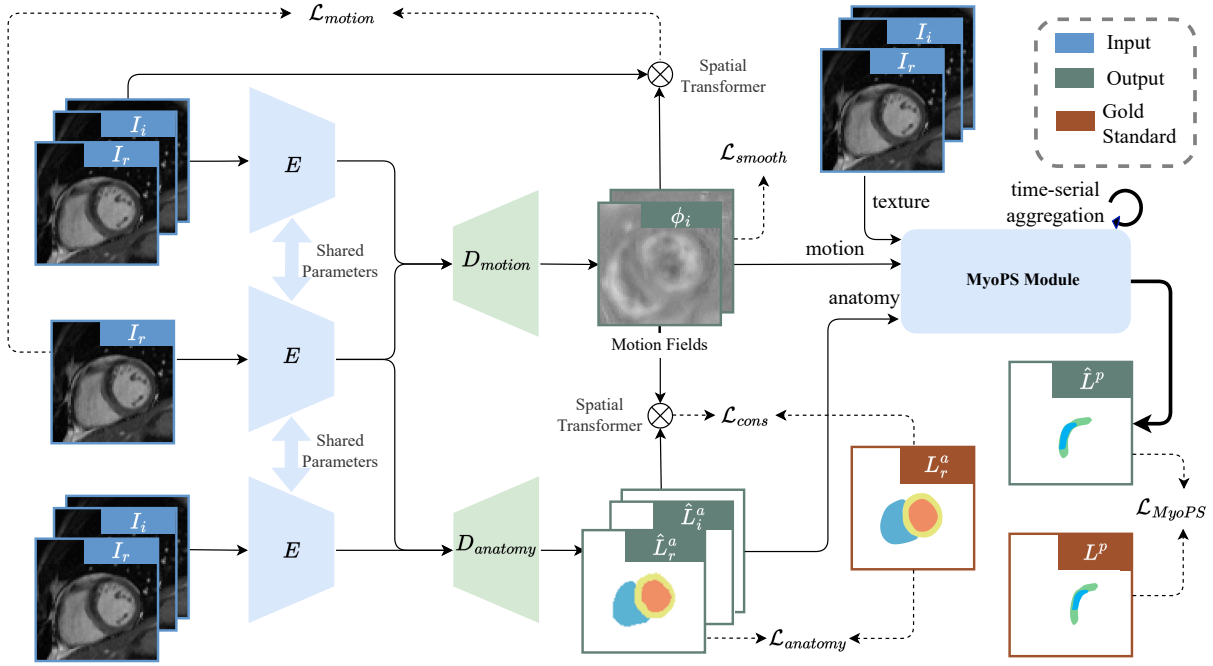


Fig. 2: The architecture of the myocardial pathology segmentation (MyoPS) network for cine CMR images, *i.e.*, CineMyoPS. It consists of three modules: a motion estimation module (consisting of E and D_{motion}), an anatomy segmentation module (consisting of E and $D_{anatomy}$), and a MyoPS module. The motion estimation module extracts motion from the cine CMR images, while the anatomy segmentation module predicts myocardial structures from the same images. The MyoPS module aggregates motion, anatomy, and texture features (represented by the original cine CMR images) for pathology segmentation. For details of the MyoPS module, please refer to Fig. 4.

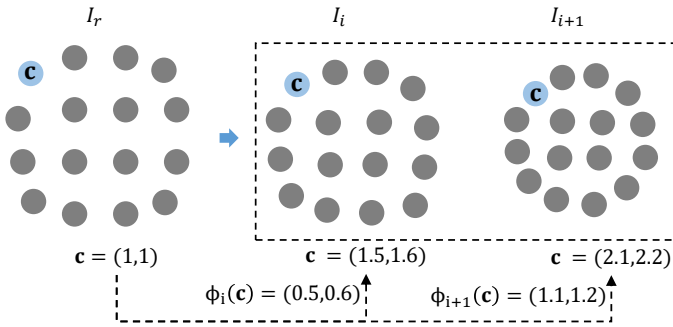


Fig. 3: A representative example of the motion field in a cine CMR sequence. Each element of the motion field (e.g. $\Phi_i(\mathbf{c})$) represents the displacement of \mathbf{c} , where (x, y) denotes its coordinates.

The motion estimation module can be trained by minimizing the difference between the reference image I_r and the moved image \tilde{I}_i :

$$\mathcal{L}_{motion} = \sum_{i=1}^n \text{MSE}(\tilde{I}_i, I_r), \quad (4)$$

where $\text{MSE}(a, b)$ computes the mean square error between a and b . Meanwhile, we constrain the smoothness of Φ_i through

a regularization term:

$$\mathcal{L}_{smooth} = \sum_{i=1}^n \|\nabla \Phi_i\|_2^2, \quad (5)$$

B. Anatomy Segmentation and Consistency Loss

MI often induces geometric remodeling of the left ventricle, leading to myocardial wall thinning [32]. We introduce an anatomy segmentation module to extract myocardial structures from the cine CMR sequences. The backbone of the module is a U-shaped segmentation subnetwork [26]. It takes I_i as input and predicts segmentation as follows:

$$\hat{L}_i^a = \mathcal{F}_{anatomy}(I_i), \quad (6)$$

where \hat{L}_i^a denotes the predicted segmentation result of I_i . The parameters of the anatomy segmentation module can be trained by minimizing the difference between the predicted and gold standard segmentation of I_i . However, delineating all frames in a cine CMR sequence is time-consuming, as each sequence typically contains 25 to 30 frames. To address this, we delineate only the anatomical label of the ED frames, and introduce a consistency loss to regularize the segmentation results across the cardiac cycle.

Specifically, we first train the anatomy segmentation module using a supervised loss:

$$\mathcal{L}_{anatomy} = -\text{Dice}(\hat{L}_r^a, L_r^a) - \text{CE}(\hat{L}_r^a, L_r^a), \quad (7)$$

where $\text{Dice}(a, b)$ and $\text{CE}(a, b)$ compute the Dice score and cross-entropy between a and b , respectively. L_r^a is the gold standard label of I_r . Then, given an unlabeled image I_i , we assume the anatomy of I_i (i.e., \hat{L}_i^a), should be consistent with that of I_r (i.e., L_r^a), after transforming it with Φ_i . We follow the joint segmentation and motion estimation schema previously proposed in the literature [33], [34], and further explore a consistency loss based on cosine distance as follows:

$$\mathcal{L}_{cons} = 1 - \cos(\hat{L}_i^a \otimes \Phi_i, \hat{L}_r^a), \quad (8)$$

where $\cos(a, b)$ measures the cosine similarity between a and b . Finally, \mathcal{L}_{cons} and $\mathcal{L}_{anatomy}$ are jointly leveraged to train the motion estimation and anatomy segmentation modules.

C. Myocardial Pathology Segmentation

Motion and anatomy features are strongly associated with myocardial pathologies, as MI often induces abnormal motion patterns and thinning of the myocardial wall. Meanwhile, texture features derived from the cine CMR sequences exhibit T1- and T2-weighted characteristics, which may contribute to the performance of MyoPS [35], [36]. We introduce a MyoPS module that integrates these features to segment scarring and edema areas. In addition, the module is designed to effectively fuse time-series information from cine CMR images to enhance segmentation performance.

Fig. 4 shows the architecture of the MyoPS module, which is a U-shaped segmentation subnetwork [26]. For each set of features extracted from the i -th frame of \mathbf{I} , i.e., Φ_i , \hat{L}_i^a and I_i , the MyoPS module takes them as inputs and predicts myocardial pathologies in the reference image space as follows:

$$\hat{L}_i^p = \mathcal{F}_{MyoPS}([\Phi_i, \hat{L}_i^a \otimes \Phi_i, I_i \otimes \Phi_i]), \quad (9)$$

where \hat{L}_i^p denotes the predicted MyoPS result of the i -th frame, $[\dots]$ represents the concatenation operation. Note that segmentation is performed in the reference image space. The MyoPS module transforms the anatomy (\hat{L}_i^a) and texture I_i by the motion field (Φ_i) to mitigate spatial misalignment with the reference image I_r .

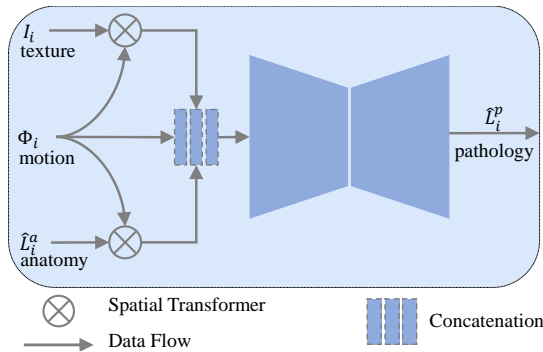


Fig. 4: The segmentation network architecture of the MyoPS module. It takes various types of features as inputs, including motion, texture, and anatomy, to perform MyoPS in a reference image space.

Furthermore, the MyoPS module can aggregate time-series information for segmentation. Given n sets of Φ_i , \hat{L}_i^a , and

I_i , the module generates n potential results across the cardiac cycle. These time-series results are subsequently integrated to obtain the final segmentation as follows:

$$\hat{L}^p = \text{Softmax}(\text{conv}(\sum_i^n \hat{L}_i^p)), \quad (10)$$

where \hat{L}^p denotes the final MyoPS result, and $\text{conv}(\dots)$ represents a convolution operation.

Having \hat{L}^p estimated, the network parameters of the MyoPS module can be trained as follows:

$$\mathcal{L}_{MyoPS} = -\text{Dice}(\hat{L}^p, L^p) - \text{CE}(\hat{L}^p, L^p), \quad (11)$$

where L^p denotes the gold standard myocardial pathology label of the reference image I_r .

Finally, we jointly train the myocardial motion estimation, anatomy segmentation, and MyoPS modules in an end-to-end manner. The overall loss function of CineMyoPS is as follows:

$$\mathcal{L} = \mathcal{L}_{MyoPS} + \lambda_1 \mathcal{L}_{anatomy} + \lambda_2 \mathcal{L}_{cons} + \lambda_3 \mathcal{L}_{motion} + \lambda_4 \mathcal{L}_{smooth}, \quad (12)$$

where λ_1 , λ_2 , λ_3 , and λ_4 are the hyperparameters.

III. EXPERIMENTS

This section first introduces the experimental datasets, implementation details, and evaluation metrics. Next, we conduct parameter and ablation studies for frame interval selection, feature effectiveness investigation, and consistency loss evaluation. Following this, we compare CineMyoPS to state-of-the-art methods. Finally, we assess the clinical quantification capabilities of our method.

A. Datasets

We evaluated CineMyoPS on a multi-center dataset, which includes three centers referred to as Center-M, Center-R, and Center-Z. The dataset contains MS-CMR sequences (i.e., cine, LGE, and T2w) from 145 MI patients. Tables I and Table II provide the demographic information of the patients and the acquisition parameters of the CMR sequences, respectively. Each case was independently annotated by two experienced raters. Annotations agreed upon by both raters were accepted as the gold standard, while disagreements were resolved by a senior radiologist specializing in cardiac imaging.

The gold standard pathologies (L^p) were generated by fusing the pathology labels from LGE and T2w images. As shown in Fig. 5, we first annotated scar and edema labels in LGE and T2w images, respectively. Then, we registered the two images to the ED phase of the cine CMR sequence from the same subject using the MvMM tool [37]. In this step, structural information from all three image modalities was utilized to ensure accurate registration. Finally, the registered labels were fused to produce the gold standard.

In the experiments, Center-M and Center-Z were randomly divided into a training set of 75 subjects and a validation set of 20 subjects, while Center-R was used for testing. The parameter and ablation studies (see Section III-C) were conducted on the validation dataset. The comparative and clinical quantification studies (see Section III-D and Section III-E) were performed on the testing dataset.

TABLE I: Demographic information of Center-M, Center-Z, and Center-R. PRE and POST refer to whether the cine images were acquired pre-contrast or post-contrast. SBP: systolic blood pressure; DBP: diastolic blood pressure; HR: heart rate; TR: training; VA: validation; TE: testing. Num: number. Male values are reported as the “number of male cases (percentage%)” format. Age, weight, SBP, DBP, and HR values are presented as the “median [min, max]” format. NA: Not available.

	Center-M	Center-Z	Center-R
Num	45	50	50
Contrast	PRE & POST	POST	PRE
Male	45 (100%)	48 (96%)	40 (80%)
Age	57 [38, 69]	56 [28, 69]	60 [36,77]
Weight (kg)	75 [60, 90]	71 [54,102]	72 [50,90]
SBP(mmHg)	NA	120 [92,186]	NA
DBP(mmHg)	NA	76 [48,113]	NA
HR	NA	78 [55,114]	NA
TR/VA/TE	35/10/0	40/10/0	0/0/45

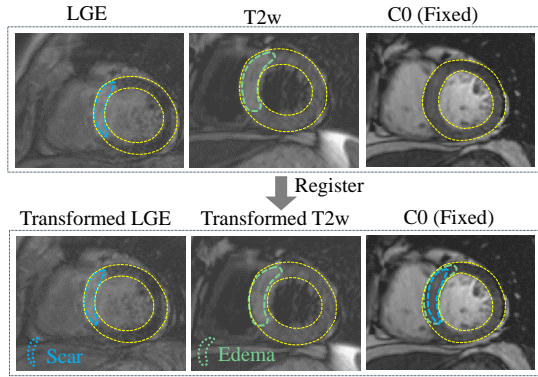


Fig. 5: Illustration of the gold standard myocardial pathology label generation process. C0: End-diastolic frame of the cine CMR sequence.

B. Implementation and Evaluation Metrics

CineMyoPS was implemented in PyTorch and trained using an RTX 4090 GPU¹. The loss function of CineMyoPS consists of four hyperparameters [see Equation (12)]. For each hyperparameter, we began with a coarse search over predefined values (0.01, 0.1, 1, 10, 100). The parameter value was initially identified based on the Dice score of scar and edema segmentation in the validation set. Subsequently, a fine-grained linear search was conducted within a range, from the identified value to five times the identified value, to determine the optimal one. The final hyperparameters of the overall loss function (12) λ_1 , λ_2 , λ_3 , and λ_4 were set to 5, 2, 1, and 100, respectively.

To evaluate the performance of CineMyoPS, the Dice score and Hausdorff distance (HD) were calculated between the predicted results and the gold standards. Additionally, sensitivity (Sen), precision (Pre), specificity (Spe), and negative predictive

value (NPV) were included to assess the effectiveness of the method. Note that we referred to the myocardium as the negative class when calculating Spe and NPV. Furthermore, we evaluated the performance of CineMyoPS with a clinical index, *i.e.*, transmuralty.

C. Parameter and Ablation Study

1) Frame Interval Study: Cine CMR sequences typically comprise 25 to 30 frames per cardiac cycle. We investigated the optimal number of frames required for MyoPS. In our experiment, we set the reference image as the starting point and extracted 1/6, 2/6, 3/6, 4/6, 5/6, and 6/6 of the frames within the cardiac cycle. By varying these proportions, CineMyoPS can aggregate time-series features relevant to the AAR. Fig. 6 illustrates the performance of CineMyoPS on the validation dataset. The results indicate that CineMyoPS initially improved with an increasing number of frames and reached a plateau when 4/6 of the total frames were used. Therefore, we adopted 4/6 of the frames from each cine CMR sequence for MyoPS in subsequent experiments, as this configuration reached an optimal balance between information richness and computational efficiency.

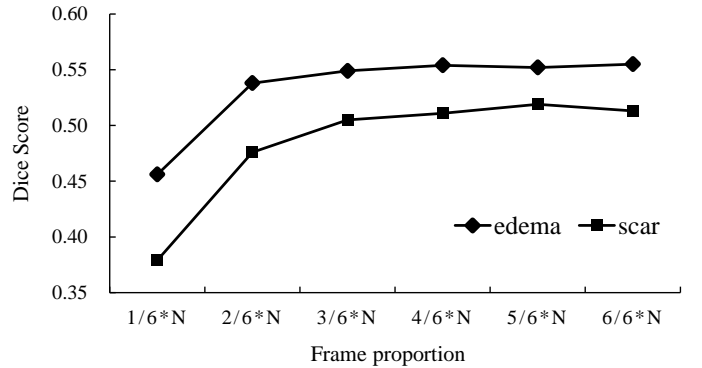


Fig. 6: Performance of CineMyoPS with different frame proportions. The average Dice scores of scar and edema were computed on the validation dataset.

2) Feature Effectiveness Study: Motion, anatomy, and texture are correlated with MI. We implemented variants of CineMyoPS to verify the effectiveness of different features. Here, we adjusted the MyoPS module of CineMyoPS by combining different features. Note that we transformed texture and anatomy features using motion fields before feeding them into the MyoPS module (see Fig. 4).

- **MyoPS_{IΦL}:** The full version of CineMyoPS, where the MyoPS module utilizes all features: motion (Φ), anatomy (L) and texture (I).
- **MyoPS_Φ, MyoPS_I and MyoPS_L:** Variants of CineMyoPS where the MyoPS module utilizes a single type of feature, such as Φ , I, or L.
- **MyoPS_{IΦ}, MyoPS_{IL} and MyoPS_{ΦL}:** Variants of CineMyoPS where the MyoPS module utilizes two types of features.

The upper panel of Table III shows the results of CineMyoPS variants where the MyoPS module utilized a single

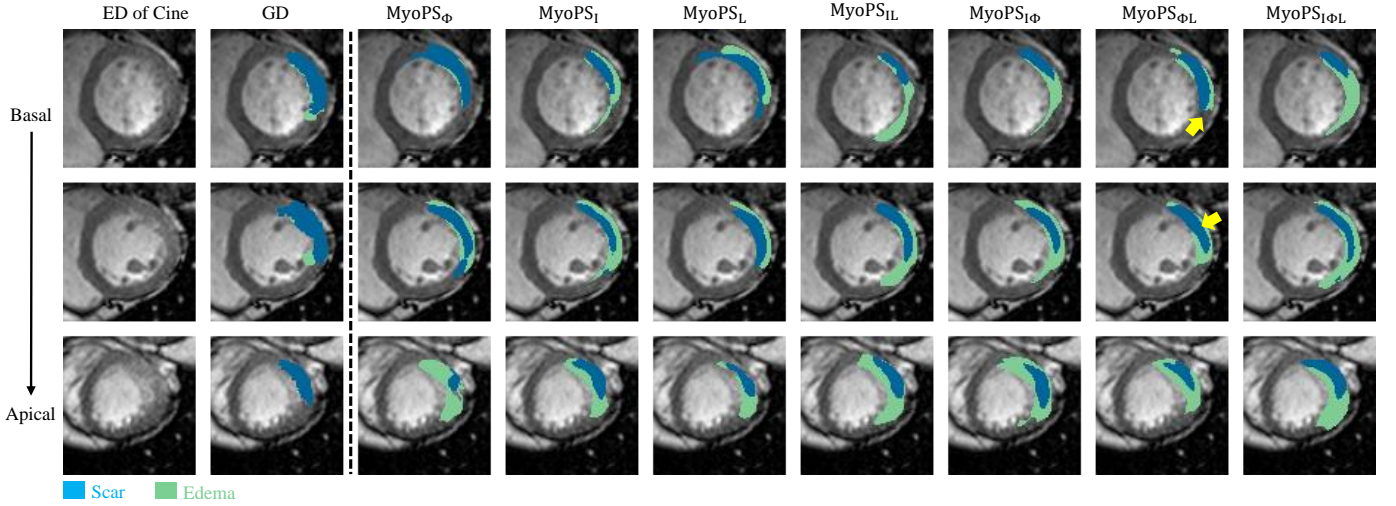
¹Source code will be released publicly at <https://github.com/NanYoMy/CineMyoPS> once the manuscript is accepted.

TABLE II: Acquisition parameters of multi-sequence CMR. Seqs: sequence, SPC: slice spacing (thickness + gap).

Seqs	In-plane resolution (mm ²)	SPC (mm)	Slice Num	Frame Num
Center-M				
Cine	$1.19 \times 1.19 \sim 1.25 \times 1.25$	12 ~ 23	2 ~ 6	30
T2w	$0.73 \times 0.73 \sim 0.76 \times 0.76$	12 ~ 20	2 ~ 6	1
LGE	$0.73 \times 0.73 \sim 0.76 \times 0.76$	11 ~ 23	2 ~ 6	1
Center-R				
Cine	1.17×1.17	6	5 ~ 15	30
LGE	0.89×0.89	10	3 ~ 12	1
T2w	0.89×0.89	10 ~ 17	3 ~ 11	1
Center-Z				
Cine	$1.77 \times 1.77 \sim 2.13 \times 2.13$	10	2 ~ 7	25
LGE	$1.33 \times 1.33 \sim 1.86 \times 1.86$	10	4 ~ 11	1
T2w	$1.33 \times 1.33 \sim 2.24 \times 2.24$	10	2 ~ 10	1

TABLE III: Performance of CineMyoPS with different feature inputs to the MyoPS module. The results were evaluated on the validation dataset. “I”, “Φ”, and “L” indicate texture, motion, and anatomy features, respectively. The best results are highlighted in **bold**. Asterisks (*) indicate significant differences between MyoPS_Φ and all other methods in the upper panel, while daggers (†) indicate differences between MyoPS_{ΦL} and all other methods in the lower panel. The number of symbols represents the level of significance: * for $p < 0.05$, ** for $p < 0.01$, † for $p < 0.05$ and ‡ for $p < 0.01$.

Methods	Features			Scar						Edema					
	I	Φ	L	Dice ↑	Pre ↑	Sen ↑	Spe ↑	NPV ↑	HD (mm) ↓	Dice ↑	Pre ↑	Sen ↑	Spe ↑	NPV ↑	HD (mm) ↓
MyoPS _I	✓	×	×	0.41 ± 0.17 *	0.66 ± 0.21	0.32 ± 0.16 *	0.94 ± 0.04	0.77 ± 0.08 *	26.47 ± 12.77	0.50 ± 0.16 *	0.76 ± 0.14	0.41 ± 0.17 *	0.89 ± 0.09	0.64 ± 0.12 **	28.13 ± 10.65
MyoPS _L	×	×	✓	0.45 ± 0.17	0.71 ± 0.16	0.36 ± 0.17	0.94 ± 0.04	0.78 ± 0.08	25.01 ± 11.26	0.55 ± 0.12 *	0.77 ± 0.12 *	0.47 ± 0.14	0.88 ± 0.07	0.66 ± 0.12 **	26.84 ± 12.28
MyoPS _Φ	×	✓	×	0.47 ± 0.15	0.72 ± 0.15	0.38 ± 0.16	0.94 ± 0.03	0.79 ± 0.07	25.05 ± 10.11	0.58 ± 0.12	0.79 ± 0.10	0.50 ± 0.15	0.89 ± 0.06	0.68 ± 0.12	23.85 ± 10.36
MyoPS _{IL}	✓	×	✓	0.42 ± 0.15 ‡	0.68 ± 0.18	0.32 ± 0.14 ‡	0.94 ± 0.04	0.77 ± 0.08 ‡	27.44 ± 11.79 ‡	0.50 ± 0.15 ‡	0.78 ± 0.15	0.41 ± 0.16 ‡	0.91 ± 0.06	0.65 ± 0.12 ‡	25.99 ± 11.25
MyoPS _{IΦ}	×	✓	✓	0.48 ± 0.16 ‡	0.71 ± 0.17	0.39 ± 0.16 ‡	0.94 ± 0.04	0.79 ± 0.07 ‡	24.22 ± 11.17 ‡	0.56 ± 0.14 ‡	0.80 ± 0.11	0.47 ± 0.17 ‡	0.90 ± 0.06	0.67 ± 0.12 ‡	23.72 ± 10.89
MyoPS _{ΦL}	✓	✓	×	0.54 ± 0.14	0.73 ± 0.14	0.46 ± 0.18	0.93 ± 0.05	0.81 ± 0.07	20.69 ± 9.13	0.60 ± 0.13	0.82 ± 0.08	0.51 ± 0.16	0.90 ± 0.06	0.69 ± 0.12	22.68 ± 8.60
MyoPS _{IΦL}	✓	✓	✓	0.51 ± 0.13	0.72 ± 0.16	0.43 ± 0.14	0.93 ± 0.04	0.80 ± 0.06 †	24.34 ± 10.56 †	0.56 ± 0.13 ‡	0.79 ± 0.11	0.48 ± 0.16 †	0.90 ± 0.06	0.67 ± 0.12 ‡	23.38 ± 10.23

**Fig. 7:** Visualization of MyoPS results by using different features. Yellow arrows indicate the regions where the methods achieved better results than other methods. GD: gold standard.

feature. MyoPS_Φ achieved the best Dice, Pre, Sen, Spe, and NPV among all methods. For scar segmentation, MyoPS_Φ achieved a Dice score that was 0.06 ($p < 0.05$) higher than MyoPS_I. For edema segmentation, MyoPS_Φ achieved Dice scores that were 0.08 ($p < 0.05$) and 0.03 ($p < 0.05$) higher than those of MyoPS_I and MyoPS_L, respectively. These results demonstrated that motion is more effective than texture and anatomy features.

The lower panel of Table III shows the results of CineMyoPS where the MyoPS module utilized multiple features. Four combinations of I, Φ, and L were evaluated

for MyoPS. Among all combinations, MyoPS_{ΦL} achieved the best performance (*i.e.*, Dice, Pre, Sen, NPV, and HD) by leveraging motion and anatomy features. Notably, MyoPS_{ΦL} significantly outperformed the other methods in Dice score for edema segmentation ($p < 0.05$). This finding highlights the effectiveness of integrating motion and anatomy features for MyoPS. Consequently, we adopted motion and anatomy features for MyoPS in the following sections.

Interestingly, incorporating more features did not always benefit MyoPS. For example, adding texture features to MyoPS_{ΦL} resulted in a statistically significant reduction of

0.04 ($p < 0.01$) in the Dice score for edema segmentation. This discrepancy arises because the texture feature may become redundant when anatomy and motion features are already present. Therefore, adding the texture feature may not always improve overall performance.

Fig. 7 shows a typical case of MyoPS results. In the basal and middle slices, MyoPS_{ΦL} produced visually better results than the other methods. This is consistent with the quantitative results of Table III. In the apical slices, the CineMyoPS variants tended to produce false positive edema regions, illustrating the challenges of performing accurate MyoPS in these areas.

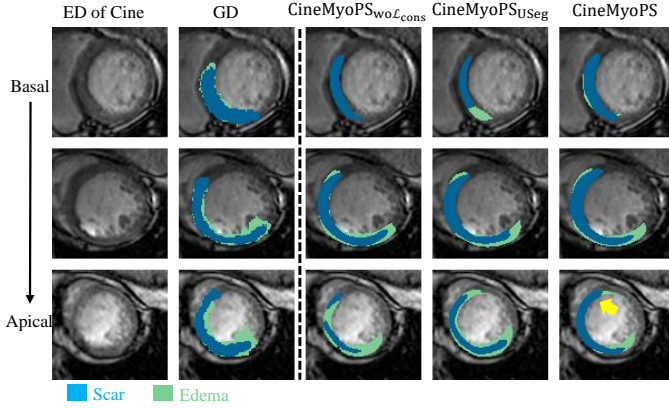


Fig. 8: Visualization of myocardial segmentation results for variants of CineMyoPS. The yellow arrows mark the areas where CineMyoPS achieved better performance than other variants.

TABLE IV: Performance of different variants of CineMyoPS for scar and edema segmentation. Asterisks (*) indicate statistically significant differences between CineMyoPS and all other methods. The number of asterisks represents the level of significance: * for $p < 0.05$ and ** for $p < 0.01$.

Methods	Scar (Dice) \uparrow	Edema (Dice) \uparrow
CineMyoPS _{woL_cons}	0.49 ± 0.16 **	0.57 ± 0.13
CineMyoPS _{Useg}	0.46 ± 0.15 **	0.56 ± 0.13 *
CineMyoPS	0.54 ± 0.14	0.60 ± 0.13

3) Consistency Loss and Time-series Aggregate Effectiveness Study: We implemented two variants of CineMyoPS to investigate the effectiveness of consistency loss and time-series aggregation strategy:

- CineMyoPS_{woL_cons}: A variant of CineMyoPS trained without using consistency loss.
- CineMyoPS_{Useg}: A variant of CineMyoPS where the MyoPS module was replaced by a Unet [38], one of the most straightforward models to perform segmentation in multi-task methods, as demonstrated in [39].

Table. IV lists the Dice scores of variants of CineMyoPS. Without using consistency loss, CineMyoPS suffered performance degradation (scar: 0.05, $p < 0.01$). This indicates the benefit of the consistency loss. Meanwhile, CineMyoPS obtained better results (scar: 0.08, $p < 0.01$; edema: 0.04,

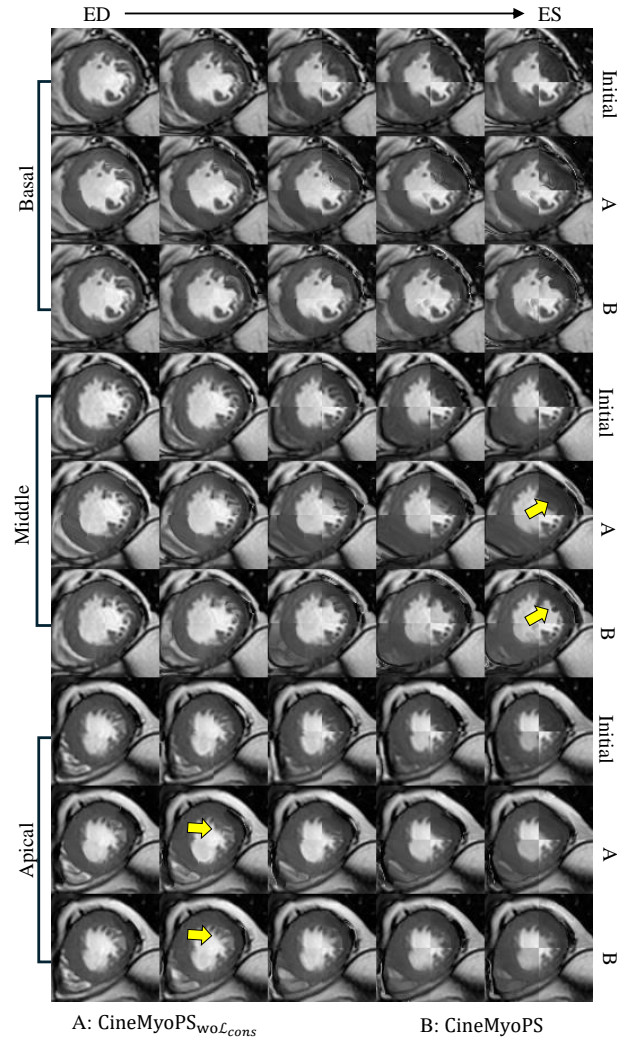


Fig. 9: Checkerboard visualization of I_r and \tilde{I}_i frames. The yellow arrows highlight the areas where CineMyoPS obtained better results than CineMyoPS_{woL_cons}. Please zoom in to view the comparison details.

$p < 0.05$) than CineMyoPS_{Useg}. This reveals that the time-series aggregation strategy can improve MyoPS. Moreover, Fig. 8 visualizes a typical case of MyoPS results. CineMyoPS achieved better segmentation details as marked by arrows, which is consistent with the quantitative results in Table. IV.

Additionally, Fig. 9 visualizes the checkerboard comparison of I_r and transformed I_i . As indicated by yellow arrows, CineMyoPS captured finer details compared to CineMyoPS_{woL_cons}. Fig. 10 shows the myocardium segmentation results of a cine CMR sequence. It is worth noting that only the reference frame labels were used to train the anatomy segmentation module of CineMyoPS. Nevertheless, CineMyoPS successfully segmented the anatomy across all frames from end-diastole to end-systole. These results demonstrate that the consistency loss enabled CineMyoPS to more accurately extract DDF (motion) and anatomy features.

D. Comparison Study

TABLE V: Performance of different cine CMR based MyoPS methods on the test dataset. The best results are highlighted in **bold**. Asterisks (*) denote statistically significant differences between CineMyoPS and all other methods. The number of asterisks represents the level of significance: * for $p < 0.05$ and ** for $p < 0.01$.

Methods	Scar						Edema					
	Dice \uparrow	Pre \uparrow	Sen \uparrow	Spe \uparrow	NPV \uparrow	HD (mm) \downarrow	Dice \uparrow	Pre \uparrow	Sen \uparrow	Spe \uparrow	NPV \uparrow	HD (mm) \downarrow
nnUnet	0.42 \pm 0.17 **	0.51 \pm 0.21 **	0.42 \pm 0.20 **	0.90 \pm 0.04	0.85 \pm 0.09 *	29.68 \pm 11.14 **	0.47 \pm 0.14 **	0.72 \pm 0.17 **	0.42 \pm 0.16 **	0.90 \pm 0.06	0.68 \pm 0.16 **	28.94 \pm 10.50 *
OFSeg	0.49 \pm 0.15 *	0.53 \pm 0.19 **	0.57 \pm 0.21	0.87 \pm 0.06 *	0.88 \pm 0.08	25.51 \pm 10.58 *	0.55 \pm 0.12	0.72 \pm 0.15 **	0.57 \pm 0.17 *	0.86 \pm 0.08 **	0.74 \pm 0.15	26.01 \pm 11.38
ConvLSTM	0.47 \pm 0.14 **	0.56 \pm 0.19 **	0.52 \pm 0.21 *	0.88 \pm 0.09 *	0.87 \pm 0.09 *	24.03 \pm 9.92 *	0.56 \pm 0.10	0.76 \pm 0.13 **	0.54 \pm 0.15	0.88 \pm 0.09 **	0.73 \pm 0.15	25.17 \pm 9.81
2D+1D Unet	0.50 \pm 0.14	0.59 \pm 0.17	0.54 \pm 0.20 *	0.90 \pm 0.06	0.87 \pm 0.08	23.47 \pm 11.74	0.56 \pm 0.09	0.78 \pm 0.13	0.53 \pm 0.15	0.90 \pm 0.07	0.72 \pm 0.15	24.65 \pm 11.19
CineMyoPS	0.53 \pm 0.12	0.60 \pm 0.18	0.57 \pm 0.19	0.90 \pm 0.07	0.88 \pm 0.09	21.40 \pm 12.24	0.57 \pm 0.08	0.79 \pm 0.13	0.53 \pm 0.14	0.91 \pm 0.07	0.72 \pm 0.14	24.24 \pm 11.71

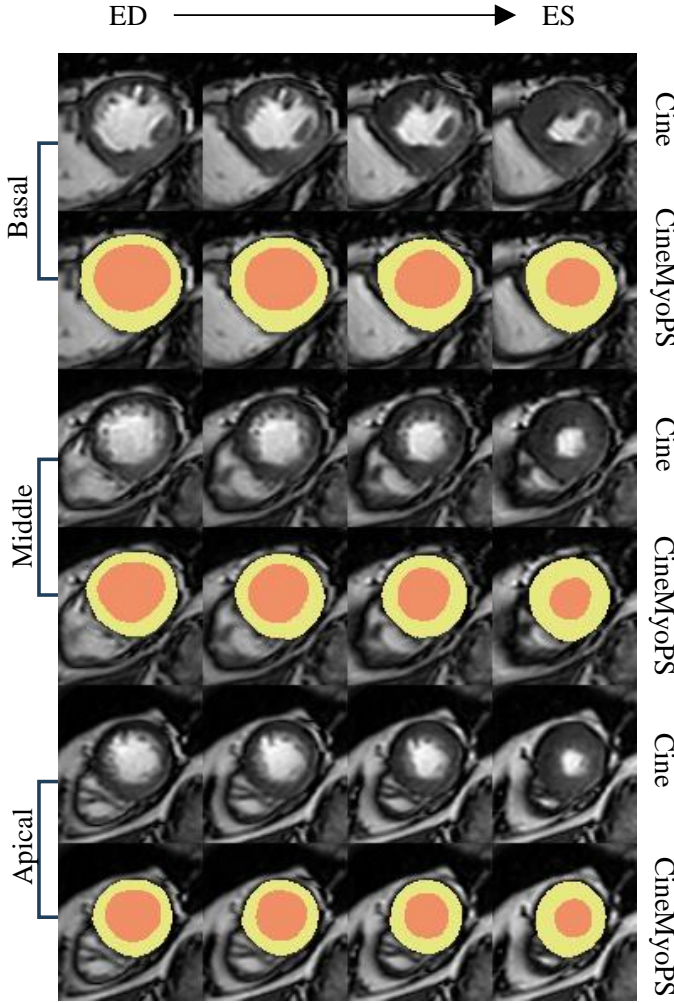


Fig. 10: Visualization of myocardial segmentation results from a cine CMR sequence. The segmentation results were generated by the anatomy segmentation module of CineMyoPS.

1) MyoPS Performance Study: We implemented four alternative MyoPS methods and compared them with the proposed CineMyoPS to assess its effectiveness.

- nnUnet: A state-of-the-art segmentation network that directly performs MyoPS from the ED phase of Cine CMR images.
- OFSeg: A segmentation network that predicts myocardial pathologies based on myocardial motion [20]. In this method, motion features are extracted using an optical flow (OF) method [40].
- ConvLSTM: A segmentation network that employs con-

volutional LSTM layers to capture spatio-temporal features for MyoPS [23].

- 2D+1D Unet: A U-shaped segmentation network that predicts myocardial pathologies by integrating 2D-spatial and 1D-temporal features [41].

The training loss of CineMyoPS is described by Equation (12), while the training loss for the comparison methods is given by Equation (11). Both CineMyoPS and comparison methods were trained with the same strategy, including the optimizer and learning rate settings, as outlined in nnUnet [38].

Table V shows the results of different MyoPS methods. CineMyoPS achieved a 0.11 ($p < 0.01$) higher Dice score for scar segmentation compared to nnUnet. Compared to the conventional OFSeg method, CineMyoPS achieved better performance in terms of Pre and Spe. Moreover, CineMyoPS estimated motion and performed MyoPS in an end-to-end manner, which simplified the procedure of MyoPS. Although 2D+1D Unet and ConvLSTM also extracted spatial features and integrated them along the temporal axis for MyoPS, they were less effective compared to CineMyoPS. For example, CineMyoPS achieved improvements in Sen of 0.05 ($p < 0.01$) and 0.03 ($p < 0.01$) over ConvLSTM and 2D+1D Unet, respectively, for scar segmentation. This indicates the effectiveness of the proposed method.

Fig. 11 shows the visual results of different methods. In general, CineMyoPS achieved better visual results than other methods for scar segmentation, as indicated by yellow arrows. However, CineMyoPS may fail to accurately segment edema, as indicated by red arrows. This is because the motion patterns of scar tissue are more distinguishable from healthy tissue than those of edema.

2) Related studies from literature: Table VI summarizes current MyoPS studies in the literature, including contrast and non-contrast methods. The upper panel lists contrast methods that perform joint scar and edema segmentation. Methods employing contrast-enhanced CMR show promising results, as they are consistent with current clinical settings, *i.e.*, with LGE CMR. Meanwhile, the performance of contrast methods was better than that of CineMyoPS, highlighting the need for enhancements in CineMyoPS to achieve comparable efficacy.

The lower panel lists non-contrast methods that primarily focus on scar segmentation. Interestingly, some of these methods not only outperformed CineMyoPS but also exhibited superior results compared to contrast methods. For instance, PSCGAN achieved 0.932 for scar segmentation, while UESTC (a contrast method) and CineMyoPS (our non-contrast method) obtained 0.64 and 0.53, respectively. This variation in performance is largely attributed to the differences between

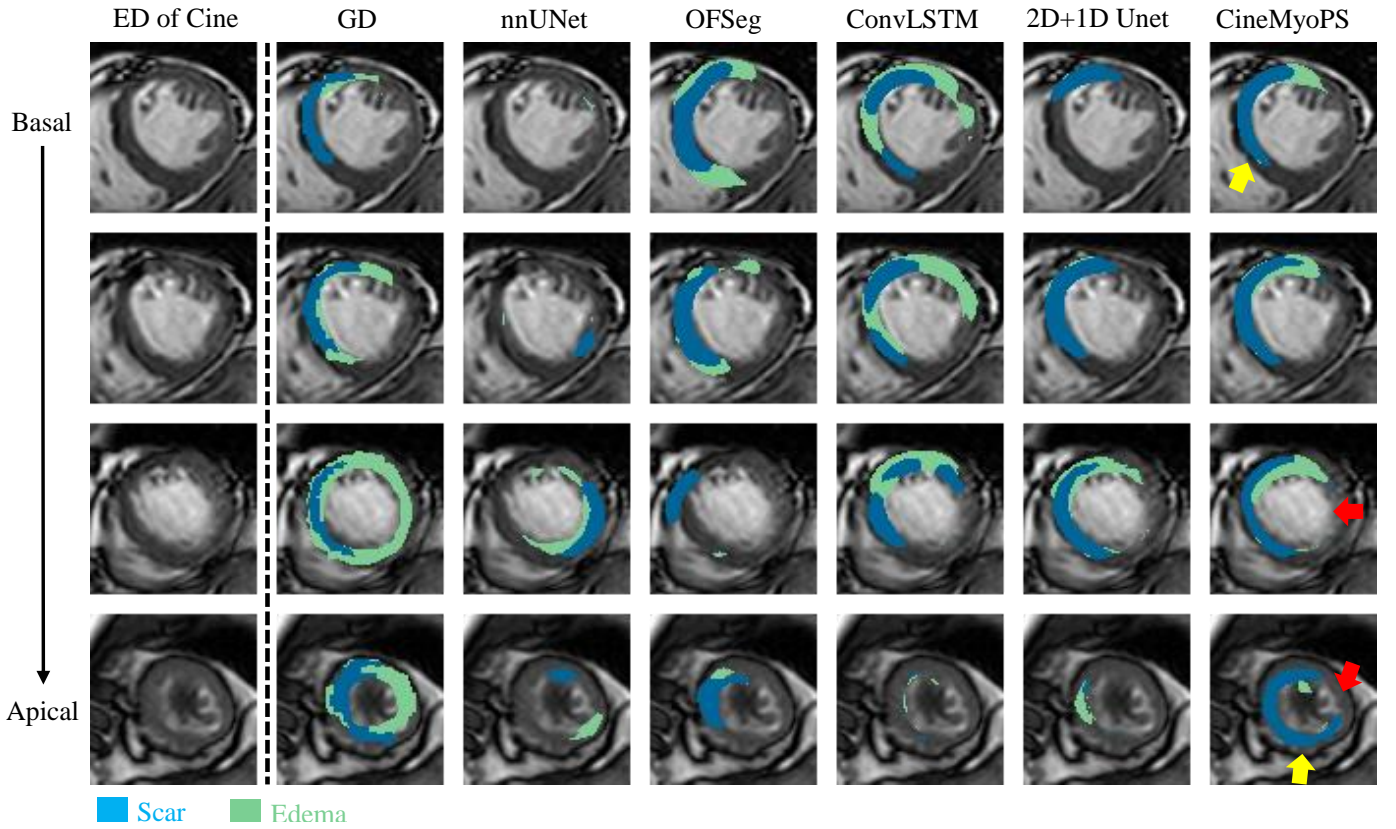


Fig. 11: Visualization results of different MyoPS methods. Yellow arrows indicate the regions where CineMyoPS achieved more plausible results than other methods. Red arrows mark the segmentation errors of CineMyoPS.

datasets. Our dataset presents challenges, as reflected by our inter-observer analysis, which yielded average Dice scores of 0.69 for scar segmentation and 0.73 for edema segmentation. Furthermore, we recruited an additional observer to perform MyoPS. The observer achieved Dice scores of 0.73 and 0.75 for scar and edema segmentation, respectively, compared to the gold standard labels. These results highlight the inherent difficulty of the MyoPS task.

TABLE VI: Summary of representative MyoPS studies in the literature. Methods in the upper panel utilize contrast-enhanced CMR sequences, while those in the lower panel rely solely on non-contrast CMR sequences. The performance of reported studies are directly obtained from the original publications.

Study	Scar (Dice) \uparrow	Edema (Dice) \uparrow
UESTC [42], contrast	0.64	0.70
UMyoPS [43], contrast	0.65	0.73
MyoPS-Net [44], contrast	0.66	0.74
PSCGAN [21], non-contrast	0.93	-
MuTGAN [45], non-contrast	0.90	-
MI-Segmentation [20], non-contrast	0.86	-
CineMyoPS, non-contrast	0.53	0.57

E. Clinical Quantification Study

We further evaluated the performance of CineMyoPS using a clinically relevant index, *i.e.*, scar transmural. To calculate transmural, we adopted a chord method [46], which divides

the myocardium into 100 equally spaced chords. The transmural of each chord was quantified as (scar pixels / chord pixels) $\times 100\%$. Each chord was classified into one of the four types according to its transmural: viable (0 ~ 25%), likely viable (26% ~ 50%), likely nonviable (51% ~ 75%), and nonviable (76% ~ 100%) [47].

Fig. 12 shows the scar transmural assessment results. CineMyoPS achieved a strong correlation with manual delineation in viable regions ($R=0.85$, $p < 0.01$). It also demonstrated moderate correlations in likely nonviable ($R=0.67$, $p < 0.01$) and likely viable regions ($R=0.67$, $p < 0.01$). However, CineMyoPS was unsuccessful in estimating scar transmural in nonviable myocardium ($R=0.22$, $p = 0.17$). These findings suggest that although CineMyoPS is capable of identifying scar regions, its accuracy in delineating the full extent of scar tissue remains limited.

Additionally, Fig. 13 illustrates the transmural of two typical scar cases. CineMyoPS achieved comparable visual results with manual delineation in basal and middle slices. However, as indicated by yellow arrows, its performance declined in the apical slices, which are commonly considered challenging cases for MyoPS [5]. Thus, CineMyoPS requires further improvement in apical slices.

IV. DISCUSSION AND CONCLUSION

This work introduces a novel framework (CineMyoPS) to assess the AAR in MI patients. It explores the potential of

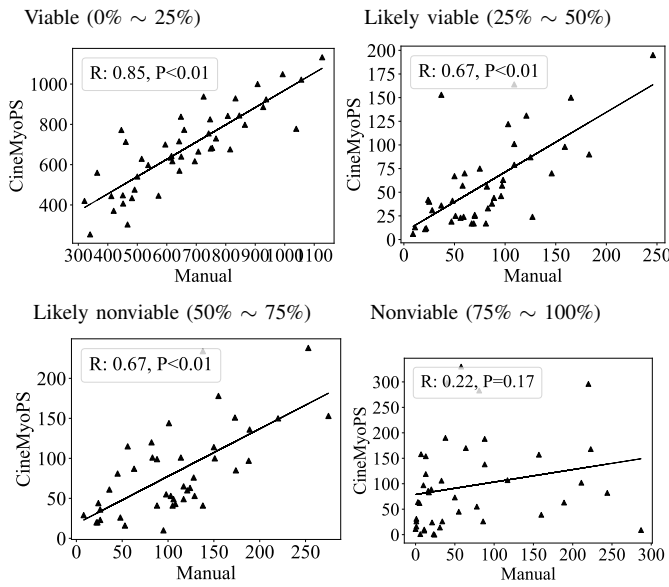


Fig. 12: Assessment of CineMyoPS for transmurality estimation. We counted the number of chords within each transmurality category, and analyzed the correlation between CineMyoPS and manual delineation. R: Pearson correlation coefficients; P: statistical significance.

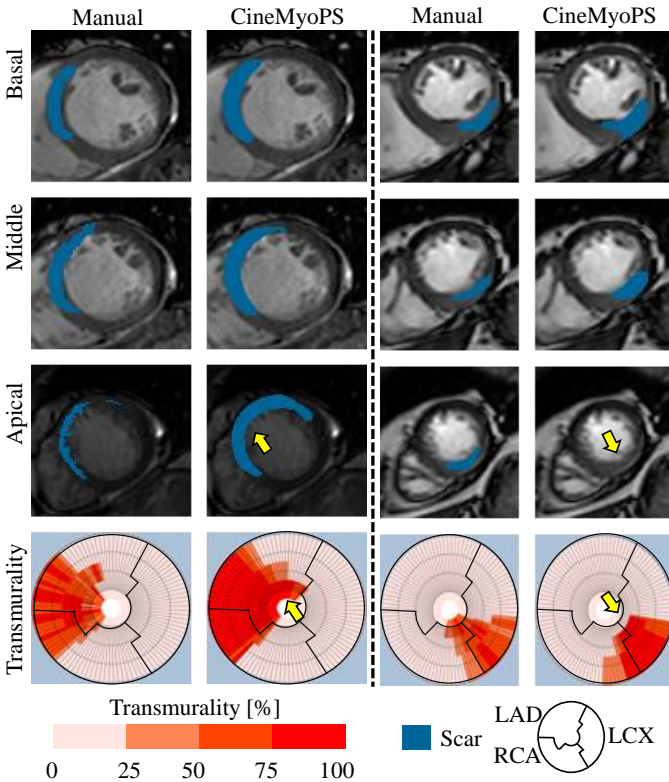


Fig. 13: Visualization of two representative scars and their transmurality. Each chord is color-coded according to its transmurality. Yellow arrows indicate areas where CineMyoPS exhibited inaccurate transmurality estimations. Bull's-eye plots in the final row depict the transmurality of each subject. LAD: left anterior descending artery; LCX: left circumflex artery; RCA: right coronary artery.

replacing LGE and T2-weighted images with cine CMR images, aiming to shorten the acquisition time of MS-CMR and eliminate the injection of contrast agents. Although contrast agents can enhance image quality, they present significant disadvantages, including potential risks of gadolinium deposition and cross-reactivity. CineMyoPS explicitly captures motion, anatomy, and texture features from cine CMR images, allowing for a comprehensive assessment of myocardial pathologies. This not only enhances patient safety but also streamlines the clinical workflow.

In the literature, motion has been widely explored for scar segmentation [20]. Meanwhile, since MI induces myocardial remodeling, anatomy is also important for MyoPS [48], [49]. Our experimental results align with these previous studies. Additionally, the texture of cine images may exhibit T1/T2 changes for MyoPS [35], [36]. However, our experimental results suggest that the benefits of including texture features are limited. The upper panel of Table III shows that motion is the most impactful feature, followed by anatomy, with texture being the least significant for MyoPS.

The performance of different cine CMR-based MyoPS methods is influenced by the types of features utilized. This is particularly evident in the performance variability among CineMyoPS variants and competing methods. Competing methods (such as ConvLSTM and 2D+1D Unet) shows minor differences in Table V. The main reason is that the feature extraction capabilities of the competing methods tend to be consistent. Specifically, these competing methods employed learnable techniques such as 2D+1D CNN and ConvLSTM to extract deep latent features for MyoPS. In contrast, the different combinations of explicit motion, anatomy and textural features utilized by CineMyoPS (such as MyoPS_t and $\text{MyoPS}_{\Phi L}$) lead to larger performance variability, as listed in Table III. Nevertheless, since CineMyoPS allows the flexible integration of different features, it can effectively mitigate the influence of irrelevant features on MyoPS.

Integrating temporal information improves the performance of MyoPS. Existing methods generally utilize temporal information based on spatio-temporal [50]–[52] and 4D [53] CNN techniques. We also observed that integrating time-series features further improves CineMyoPS performance. For instance, without fusing time-series information, CineMyoPS_{USeg} exhibited a decrease in Dice scores for scar and edema segmentation, as listed in Table IV. This finding is consistent with previous studies. Furthermore, we investigated the optimal amount of temporal information required for MyoPS. As shown in Figure 6, utilizing 4 out of 6 frames in a cardiac cycle is sufficient for MyoPS.

Another important point to emphasize is that CineMyoPS was trained using pre- and post-contrast cine CMR images, while testing was conducted solely with pre-contrast images. Note that most cine CMR images in clinical practice are acquired after contrast injection, resulting in texture features that exhibit the presence of contrast. As listed in Table III, CineMyoPS achieved Dice scores of 0.41 and 0.50 for the segmentation of scars and edema, respectively, when using texture features. Considering the domain gap [54] between pre-contrast and post-contrast datasets, we believe that Cine-

MyoPS can be improved by training on a larger pre-contrast cine CMR dataset.

The performance and interpretability of CineMyoPS require further enhancement for clinical translation. A notable limitation is its inaccuracies in delineating the full extent of MI areas (see Fig. 12). Meanwhile, CineMyoPS encounters substantial challenges when processing apical slices (see Fig. 7 and 13), and may fail to segment edema, as shown in Figure 11. It is worth noting that MyoPS remains a highly challenging task, as even a human observer was unable to achieve accurate consistency with the gold standard (see Section III-D.2). Thus, future work should aim to enhance the performance of CineMyoPS. Moreover, although CineMyoPS can identify the presence of scars and edema, its lack of clinical interpretability may obscure model failures. Future work could develop synergistic models for CineMyoPS, paving the way for clinical translation [55].

REFERENCES

- [1] Y. Chandrashekhar, T. Alexander, A. Mullasari, D. J. Kumbhani, S. Alam, E. Alexanderson, D. Bachani, J. C. Wilhelmus Badenhorst, R. Baliga, J. J. Bax, et al., "Resource and infrastructure-appropriate management of st-segment elevation myocardial infarction in low-and middle-income countries," *Circulation*, vol. 141, no. 24, pp. 2004–2025, 2020.
- [2] E. Dall'Armellina, N. Karia, A. C. Lindsay, T. D. Karamitsos, V. Ferreira, M. D. Robson, P. Kellman, J. M. Francis, C. Forfar, B. D. Prendergast, et al., "Dynamic changes of edema and late gadolinium enhancement after acute myocardial infarction and their relationship to functional recovery and salvage index," *Circulation: Cardiovascular Imaging*, vol. 4, no. 3, pp. 228–236, 2011.
- [3] C. W. Beijnink, N. W. van der Hoeven, L. S. Konijnenberg, R. J. Kim, S. C. Bekkers, R. A. Kloner, H. Everaars, S. El Messaoudi, A. C. van Rossum, N. van Royen, et al., "Cardiac mri to visualize myocardial damage after st-segment elevation myocardial infarction: a review of its histologic validation," *Radiology*, vol. 301, no. 1, pp. 4–18, 2021.
- [4] L. Li, W. Ding, L. Huang, X. Zhuang, and V. Grau, "Multi-modality cardiac image computing: A survey," *Medical Image Analysis*, vol. 88, p. 102869, 2023.
- [5] L. Li, F. Wu, S. Wang, X. Luo, C. Martín-Isla, S. Zhai, J. Zhang, Y. Liu, Z. Zhang, M. J. Ankenbrand, et al., "Myops: A benchmark of myocardial pathology segmentation combining three-sequence cardiac magnetic resonance images," *Medical Image Analysis*, vol. 87, p. 102808, 2023.
- [6] R. C. Cury, K. Shash, J. T. Nagurney, G. Rosito, M. D. Shapiro, C. H. Nomura, S. Abbara, F. Bamberg, M. Ferencik, E. J. Schmidt, et al., "Cardiac magnetic resonance with t2-weighted imaging improves detection of patients with acute coronary syndrome in the emergency department," *Circulation*, vol. 118, no. 8, pp. 837–844, 2008.
- [7] M. Polacin, M. Károlyi, M. Eberhard, A. Gotschy, B. Baessler, H. Alkadhi, S. Kozierke, and R. Manka, "Segmental strain analysis for the detection of chronic ischemic scars in non-contrast cardiac mri cine images," *Scientific Reports*, vol. 11, no. 1, p. 12376, 2021.
- [8] V. Gulani, F. Calamante, F. G. Shellock, E. Kanal, and S. B. Reeder, "Gadolinium deposition in the brain: summary of evidence and recommendations," *The Lancet Neurology*, vol. 16, no. 7, pp. 564–570, 2017.
- [9] F. Vega, A. A. van de Ven, and A. J. van der Molen, "Cross-reactivity in hypersensitivity reactions to contrast agents: new classification and guide for clinical practice," *European Radiology*, pp. 1–6, 2024.
- [10] H. Bulluck, M. Hammond-Haley, M. Fontana, D. S. Knight, A. Sirker, A. S. Herrey, C. Manisty, P. Kellman, J. C. Moon, and D. J. Hausenloy, "Quantification of both the area-at-risk and acute myocardial infarct size in st-segment elevation myocardial infarction using t1-mapping," *Journal of Cardiovascular Magnetic Resonance*, vol. 19, no. 1, pp. 1–11, 2017.
- [11] B. Sjøli, S. Ørn, B. Grenne, H. Ihlen, T. Edvardsen, and H. Brunvand, "Diagnostic capability and reproducibility of strain by doppler and by speckle tracking in patients with acute myocardial infarction," *JACC: Cardiovascular Imaging*, vol. 2, no. 1, pp. 24–33, 2009.
- [12] N. Duchateau, M. De Craene, P. Allain, E. Saloux, and M. Sermesant, "Infarct localization from myocardial deformation: prediction and uncertainty quantification by regression from a low-dimensional space," *IEEE transactions on medical imaging*, vol. 35, no. 10, pp. 2340–2352, 2016.
- [13] D. Peressutti, W. Bai, W. Shi, C. Tobon-Gomez, T. Jackson, M. Sohal, A. Rinaldi, D. Rueckert, and A. King, "Towards left ventricular scar localisation using local motion descriptors," in *International Workshop on Statistical Atlases and Computational Models of the Heart*, pp. 30–39, Springer, 2015.
- [14] H. Bleton, J. Margeta, H. Lombaert, H. Delingette, and N. Ayache, "Myocardial infarct localization using neighbourhood approximation forests," in *Statistical Atlases and Computational Models of the Heart. Imaging and Modelling Challenges: 6th International Workshop, STACOM 2015, Held in Conjunction with MICCAI 2015, Munich, Germany, October 9, 2015, Revised Selected Papers 6*, pp. 108–116, Springer, 2016.
- [15] G. K. Rumindo, N. Duchateau, P. Croisille, J. Ohayon, and P. Clarysse, "Strain-based parameters for infarct localization: evaluation via a learning algorithm on a synthetic database of pathological hearts," in *Functional Imaging and Modelling of the Heart: 9th International Conference, FIMH 2017, Toronto, ON, Canada, June 11–13, 2017, Proceedings 9*, pp. 106–114, Springer, 2017.
- [16] K. Mangion, C. McComb, D. A. Auger, F. H. Epstein, and C. Berry, "Magnetic resonance imaging of myocardial strain after acute st-segment-elevation myocardial infarction: a systematic review," *Circulation: Cardiovascular Imaging*, vol. 10, no. 8, p. e006498, 2017.
- [17] N. Duchateau and M. Sermesant, "Prediction of infarct localization from myocardial deformation," in *International Workshop on Statistical Atlases and Computational Models of the Heart*, pp. 51–59, Springer, 2015.
- [18] N. Duchateau, M. De Craene, G. Piella, and A. F. Frangi, "Constrained manifold learning for the characterization of pathological deviations from normality," *Medical image analysis*, vol. 16, no. 8, pp. 1532–1549, 2012.
- [19] C. Xu, J. Howey, P. Ohorodnyk, M. Roth, H. Zhang, and S. Li, "Segmentation and quantification of infarction without contrast agents via spatiotemporal generative adversarial learning," *Medical image analysis*, vol. 59, p. 101568, 2020.
- [20] N. Zhang, G. Yang, Z. Gao, C. Xu, Y. Zhang, R. Shi, J. Keegan, L. Xu, H. Zhang, Z. Fan, et al., "Deep learning for diagnosis of chronic myocardial infarction on nonenhanced cardiac cine mri," *Radiology*, vol. 291, no. 3, pp. 606–617, 2019.
- [21] C. Xu, L. Xu, P. Ohorodnyk, M. Roth, B. Chen, and S. Li, "Contrast agent-free synthesis and segmentation of ischemic heart disease images using progressive sequential causal gans," *Medical image analysis*, vol. 62, p. 101668, 2020.
- [22] Q. Chen and V. Koltun, "Full flow: Optical flow estimation by global optimization over regular grids," in *Proceedings of the IEEE conference on computer vision and pattern recognition*, pp. 4706–4714, 2016.
- [23] X. Shi, Z. Chen, H. Wang, D.-Y. Yeung, W.-K. Wong, and W.-c. Woo, "Convolutional lstm network: A machine learning approach for precipitation nowcasting," *Advances in neural information processing systems*, vol. 28, 2015.
- [24] D. Tran, L. Bourdev, R. Fergus, L. Torresani, and M. Paluri, "Learning spatiotemporal features with 3d convolutional networks," in *Proceedings of the IEEE international conference on computer vision*, pp. 4489–4497, 2015.
- [25] I. Goodfellow, J. Pouget-Abadie, M. Mirza, B. Xu, D. Warde-Farley, S. Ozair, A. Courville, and Y. Bengio, "Generative adversarial networks," *Communications of the ACM*, vol. 63, no. 11, pp. 139–144, 2020.
- [26] O. Ronneberger, P. Fischer, and T. Brox, "U-net: Convolutional networks for biomedical image segmentation," in *Medical Image Computing and Computer-Assisted Intervention—MICCAI 2015: 18th International Conference, Munich, Germany, October 5–9, 2015, Proceedings, Part III 18*, pp. 234–241, Springer, 2015.
- [27] D. P. O'Regan, B. Ariff, A. J. Baksi, F. Gordon, G. Durighel, and S. A. Cook, "Salvage assessment with cardiac mri following acute myocardial infarction underestimates potential for recovery of systolic strain," *European radiology*, vol. 23, pp. 1210–1217, 2013.
- [28] A. Kumar, R. Dharmakumar, J. Green, J. Flewitt, and M. Friedrich, "T2-component of conventional cine ssfp sequences is sufficient to detect myocardial edema in patients with acute reperfused myocardial infarction," in *Proc 16th Annual Meeting ISMRM, Toronto*, p. 2956, 2008.
- [29] J. W. Goldfarb, J. McLaughlin, C. A. Gray, and J. Han, "Cyclic cine-balanced steady-state free precession image intensity variations: Impli-

- cations for the detection of myocardial edema,” *Journal of Magnetic Resonance Imaging*, vol. 33, no. 3, pp. 573–581, 2011.
- [30] A. C. T. Rodrigues, R. Hataishi, F. Ichinose, K. D. Bloch, G. Derumeaux, M. H. Picard, and M. Scherrer-Crosbie, “Relationship of systolic dysfunction to area at risk and infarction size after ischemia-reperfusion in mice,” *Journal of the American Society of Echocardiography*, vol. 17, no. 9, pp. 948–953, 2004.
- [31] G. Balakrishnan, A. Zhao, M. R. Sabuncu, J. Guttag, and A. V. Dalca, “Voxelmorph: a learning framework for deformable medical image registration,” *IEEE transactions on medical imaging*, vol. 38, no. 8, pp. 1788–1800, 2019.
- [32] N. D’Elia, J. D’hooge, and T. H. Marwick, “Association between myocardial mechanics and ischemic lv remodeling,” *JACC: Cardiovascular Imaging*, vol. 8, no. 12, pp. 1430–1443, 2015.
- [33] C. Qin, W. Bai, J. Schlemper, S. E. Petersen, S. K. Piechnik, S. Neubauer, and D. Rueckert, “Joint learning of motion estimation and segmentation for cardiac mr image sequences,” in *Medical Image Computing and Computer Assisted Intervention—MICCAI 2018: 21st International Conference, Granada, Spain, September 16–20, 2018, Proceedings, Part II 11*, pp. 472–480, Springer, 2018.
- [34] K. Ta, S. S. Ahn, A. Lu, J. C. Stendahl, A. J. Sinusas, and J. S. Duncan, “A semi-supervised joint learning approach to left ventricular segmentation and motion tracking in echocardiography,” in *2020 IEEE 17th International Symposium on Biomedical Imaging (ISBI)*, pp. 1734–1737, IEEE, 2020.
- [35] E. Tahir, M. Sinn, S. Bohnen, M. Avanesov, D. Säring, C. Stehning, B. Schnackenburg, C. Eulenburg, J. Wien, U. K. Radunski, *et al.*, “Acute versus chronic myocardial infarction: diagnostic accuracy of quantitative native t1 and t2 mapping versus assessment of edema on standard t2-weighted cardiovascular mr images for differentiation,” *Radiology*, vol. 285, no. 1, pp. 83–91, 2017.
- [36] O. Jaubert, G. Cruz, A. Bustin, T. Schneider, P. Koken, M. Doneva, D. Rueckert, R. M. Botnar, and C. Prieto, “Free-running cardiac magnetic resonance fingerprinting: Joint t1/t2 map and cine imaging,” *Magnetic resonance imaging*, vol. 68, pp. 173–182, 2020.
- [37] X. Zhuang, “Multivariate mixture model for myocardial segmentation combining multi-source images,” *IEEE transactions on pattern analysis and machine intelligence*, vol. 41, no. 12, pp. 2933–2946, 2019.
- [38] F. Isensee, P. F. Jaeger, S. A. Kohl, J. Petersen, and K. H. Maier-Hein, “nnu-net: a self-configuring method for deep learning-based biomedical image segmentation,” *Nature methods*, vol. 18, no. 2, pp. 203–211, 2021.
- [39] I. Oksuz, J. R. Clough, B. Ruijsink, E. P. Anton, A. Bustin, G. Cruz, C. Prieto, A. P. King, and J. A. Schnabel, “Deep learning-based detection and correction of cardiac mr motion artefacts during reconstruction for high-quality segmentation,” *IEEE Transactions on Medical Imaging*, vol. 39, no. 12, pp. 4001–4010, 2020.
- [40] G. Farneback, “Two-frame motion estimation based on polynomial expansion,” in *Image Analysis: 13th Scandinavian Conference, SCIA 2003 Halmstad, Sweden, June 29–July 2, 2003 Proceedings 13*, pp. 363–370, Springer, 2003.
- [41] Z. Qiu, T. Yao, and T. Mei, “Learning spatio-temporal representation with pseudo-3d residual networks,” in *proceedings of the IEEE International Conference on Computer Vision*, pp. 5533–5541, 2017.
- [42] S. Zhai, R. Gu, W. Lei, and G. Wang, “Myocardial edema and scar segmentation using a coarse-to-fine framework with weighted ensemble,” in *Myocardial pathology segmentation combining multi-sequence CMR challenge*, pp. 49–59, Springer, 2020.
- [43] W. Ding, L. Li, J. Qiu, S. Wang, L. Huang, Y. Chen, S. Yang, and X. Zhuang, “Aligning multi-sequence cmr towards fully automated myocardial pathology segmentation,” *IEEE Transactions on Medical Imaging*, 2023.
- [44] J. Qiu, L. Li, S. Wang, K. Zhang, Y. Chen, S. Yang, and X. Zhuang, “Myops-net: Myocardial pathology segmentation with flexible combination of multi-sequence cmr images,” *Medical Image Analysis*, vol. 84, p. 102694, 2023.
- [45] C. Xu, L. Xu, Z. Gao, S. Zhao, H. Zhang, Y. Zhang, X. Du, S. Zhao, D. Ghista, H. Liu, *et al.*, “Direct delineation of myocardial infarction without contrast agents using a joint motion feature learning architecture,” *Medical image analysis*, vol. 50, pp. 82–94, 2018.
- [46] F. H. Sheehan, E. L. Bolson, H. T. Dodge, D. G. Mathey, J. Schofer, and H. Woo, “Advantages and applications of the centerline method for characterizing regional ventricular function,” *Circulation*, vol. 74, no. 2, pp. 293–305, 1986.
- [47] Q. Zhang, M. K. Burrage, M. Shanmuganathan, R. A. Gonzales, E. Lukaschuk, K. E. Thomas, R. Mills, J. Leal Pelado, C. Nikolaidou, I. A. Popescu, *et al.*, “Artificial intelligence for contrast-free mri: Scar assessment in myocardial infarction using deep learning-based virtual native enhancement,” *Circulation*, vol. 146, no. 20, pp. 1492–1503, 2022.
- [48] H. O’Brien, J. Whitaker, B. Singh Sidhu, J. Gould, T. Kurzendorfer, M. D. O’Neill, R. Rajani, K. Grigoryan, C. A. Rinaldi, J. Taylor, *et al.*, “Automated left ventricle ischemic scar detection in ct using deep neural networks,” *Frontiers in cardiovascular medicine*, vol. 8, p. 655252, 2021.
- [49] E. Avard, I. Shiri, G. Hajianfar, H. Abdollahi, K. R. Kalantari, G. Houshmand, K. Kasani, A. Bitarafan-Rajabi, M. R. Deevband, M. Oveisi, *et al.*, “Non-contrast cine cardiac magnetic resonance image radiomics features and machine learning algorithms for myocardial infarction detection,” *Computers in Biology and Medicine*, vol. 141, p. 105145, 2022.
- [50] Y. Yan, J. Cheng, X. Yang, Z. Gu, S. Leng, R. S. Tan, L. Zhong, and J. C. Rajapakse, “Coarse-grained mask regularization for microvascular obstruction identification from non-contrast cardiac magnetic resonance,” in *International Conference on Medical Image Computing and Computer-Assisted Intervention*, pp. 231–241, Springer, 2024.
- [51] J. Liu, X. Zhu, C. Xu, L. Xu, Z. Gao, K. Polat, and F. Alenezi, “Accurate 3d contrast-free myocardial infarction delineation using a 4d dual-stream spatiotemporal feature learning framework,” *Applied Soft Computing*, vol. 146, p. 110694, 2023.
- [52] H. Qi, P. Qian, L. Tang, B. Chen, D. An, and L.-M. Wu, “Predicting late gadolinium enhancement of acute myocardial infarction in contrast-free cardiac cine mri using deep generative learning,” *Circulation: Cardiovascular Imaging*, vol. 17, no. 9, p. e016786, 2024.
- [53] A. Amyar, S. Nakamori, M. Morales, S. Yoon, J. Rodriguez, J. Kim, R. M. Judd, J. W. Weinsaft, and R. Nezafat, “Gadolinium-free cardiac mri myocardial scar detection by 4d convolution factorization,” in *International Conference on Medical Image Computing and Computer-Assisted Intervention*, pp. 639–648, Springer, 2023.
- [54] Z. Su, K. Yao, X. Yang, Q. Wang, Y. Yan, J. Sun, and K. Huang, “Mind the gap: Alleviating local imbalance for unsupervised cross-modality medical image segmentation,” *IEEE Journal of Biomedical and Health Informatics*, vol. 27, no. 7, pp. 3396–3407, 2023.
- [55] J. Corral-Acero, F. Margara, M. Marciniak, C. Rodero, F. Loncaric, Y. Feng, A. Gilbert, J. F. Fernandes, H. A. Bukhari, A. Wajdan, *et al.*, “The ‘digital twin’ to enable the vision of precision cardiology,” *European heart journal*, vol. 41, no. 48, pp. 4556–4564, 2020.